Towards adaptive bioelectronic wound therapy with integrated real-time diagnostics and machine learning–driven closed-loop control

Check for updates

Houpu Li[1,8], Hsin-ya Yang[2,8], Fan Lu[3,8], Wan Shen Hee[1,8], Narges Asefifeyzabadi[1], Prabhat Baniya[1], Anthony Gallegos[2], Kaelan Schorger[1], Kan Zhu[4], Cynthia Recendez[4], Maryam Tebyani[1], Manasa Kesapragada[3], Gordon Keller[1], Sujung Kim[1], George Luka[1], Ksenia Zlobina[3], Tiffany Nguyen[1], Sydnie Figuerres[1], Celeste Franco[1], Koushik Devarajan[1], Alexie Barbee[1], Kylie Lin[4], Shannon M. Clayton[5], Annabelle Eaton[1], Elham Aslankoohi[1], Athena M. Soulika[5], Min Zhao[2,4] ✉, Mircea Teodorescu[1,6,7] ✉, Marcella Gomez[3] ✉, Roslyn Rivkah Isseroff[2] ✉ & Marco Rolandi[1,7] ✉

Impaired wound healing affects millions worldwide, especially those without timely healthcare access. Here, we have developed a portable and wireless platform for real-time, continuous, and adaptive bioelectronic wound therapy (a-Heal). The platform integrates a wearable device for wound imaging and delivery of therapy with an ML Physician. The ML Physician analyzes wound images, diagnoses the wound stage, and prescribes therapies to guide optimal healing. Bioelectronic actuators in the wearable device deliver therapies, including electric fields or drugs, dynamically in a closed-loop system. a-Heal evaluates wound progress, adapts therapy as needed, and sends updates to human physicians through a graphical user interface, which also supports manual intervention. In preliminary studies using a large animal model, a-Heal promoted tissue regeneration, reduced inflammation, and accelerated healing, highlighting its potential in personalized wound care.

The average person suffers 1–3 wounds annually, resulting in an estimated 24 billion wounds worldwide each year[1]. These wounds range from minor scrapes and traumatic injuries to surgical incisions and chronic ulcers[2]. While many wounds heal with basic at-home care, others require timely medical intervention to ensure proper healing[3]. Delays in access to healthcare can lead to complications, including scarring, permanent tissue damage, infection, sepsis, and even death[4]. Wound type and individual variability further complicate the selection of optimal treatments[5]. Traditional methods often rely on static, standardized protocols and assessments that cannot adapt to the individual patient, the type, and importantly, the changing state of a wound[6]. These deficits can result in prolonged recovery, increased risks of complications, and less-than-ideal healing outcomes[7].

Recent advances in wearables and smart bandages enable personalized wound treatment[8] using remotely controlled microneedle[9,10], photo patch[11], and wireless bandages with sensing and drug delivery function[12,13]. This treatment can be optimized through continuous wound monitoring with onboard sensors to improve delivery and outcomes[12,13]. However, wound healing is inherently complex, progressing through hemostasis, inflammation, proliferation, and maturation stages, each involving distinct cellular and biochemical processes that require adaptive therapy with specific biochemical signaling for optimal healing[6]. Incorporating sensors to monitor every biochemical process in the wound remains a challenge[14]. To address this, machine learning (ML) approaches have significantly improved healthcare by processing and inferring diagnostics from large, continuously updating datasets[15,16]. Holistic, ML-driven methods can assess the overall

[1]Department of Electrical and Computer Engineering, University of California Santa Cruz, Santa Cruz, CA, USA. [2]Department of Dermatology, School of Medicine, University of California Davis, Davis, CA, USA. [3]Department of Applied Mathematics, University of California Santa Cruz, Santa Cruz, CA, USA. [4]Department of Ophthalmology, School of Medicine, University of California Davis, Davis, CA, USA. [5]Pediatric Regenerative Medicine, Shriners Hospitals for Children, Sacramento, CA, USA. [6] Department of Biomolecular Engineering, University of California Santa Cruz, Santa Cruz, USA. [7] Genomics Institute, University of California Santa Cruz, Santa Cruz, USA. [8]These authors contributed equally: Houpu Li, Hsin-ya Yang, Fan Lu, Wan Shen Hee. ✉e-mail: minzhao@ucdavis.edu; mteodore@ucsc.edu; mgomez26@ucsc.edu; rrisseroff@ucdavis.edu; mrolandi@ucsc.edu
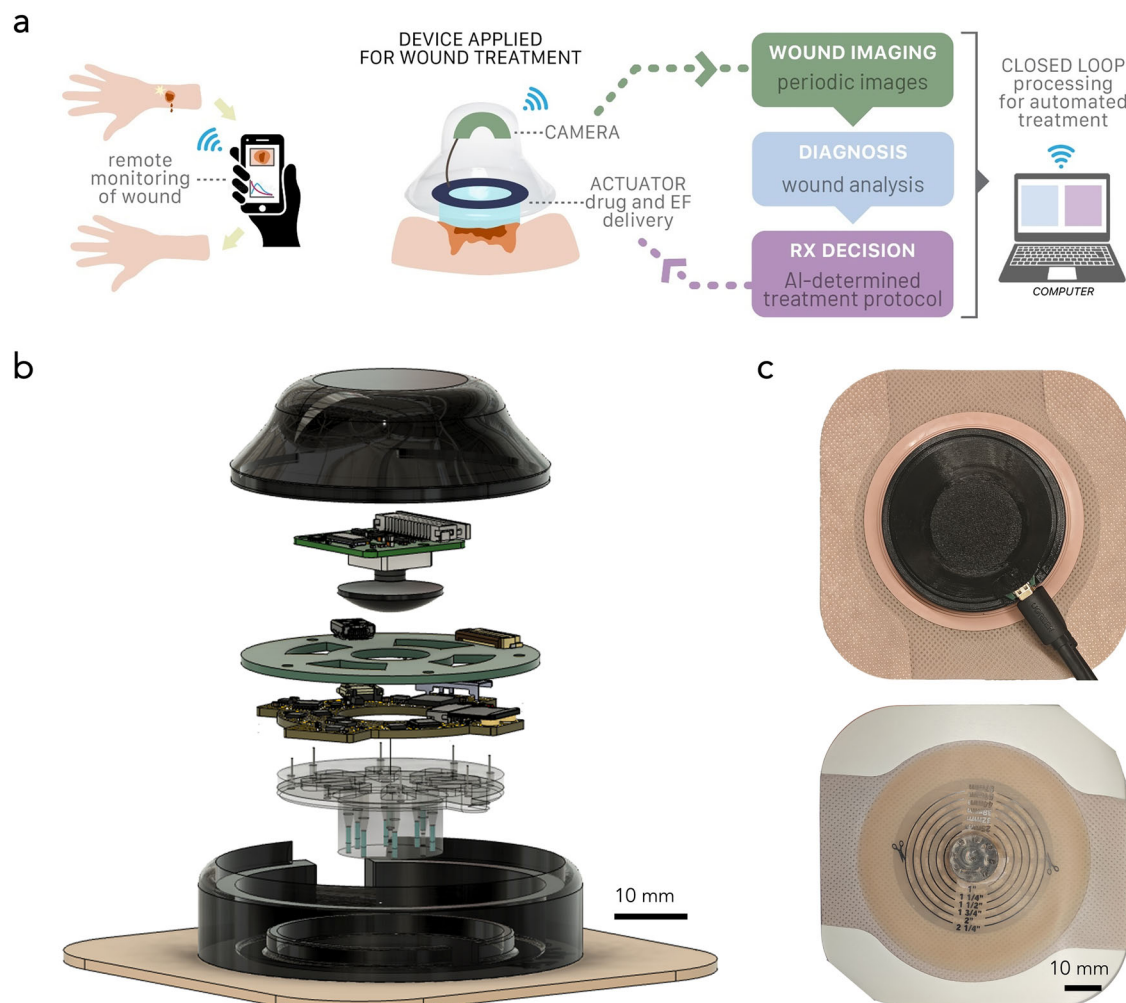
Fig. 1 | Wireless, integrated system for real-time, onboard, adaptive wound diagnostics and treatment. a There Heal platform. **b** CAD model of There Heal wearable device, illustrating the integrated camera for wound monitoring and actuator for drug delivery or stimulation. **c** Photograph of the A-Heal wearable, demonstrating the final setup with the camera and actuator, highlighting the translation of the CAD model into a functional prototype and integration with bandage for ease of application.

wound stage, indicate required treatments, and adjust them in real-time based on the wound trajectory[17,18]. Here, we introduce a wireless, integrated platform (a-Heal) for real-time, onboard, adaptive, and personalized wound diagnostics and therapy, utilizing ML to continuously determine the updated wound stages, prescribe and deliver therapies for optimized healing (Fig. 1).

Results and discussion
a-Heal
The a-Heal platform includes two main components: the a-Heal wearable device (Fig. 1 and S1), which monitors wounds and delivers on-demand therapy, and the a-Heal ML Physician, a ML driven adaptive diagnostic and treatment algorithm with a graphical user interface (GUI) for human physician oversight, if needed (Fig. 1a). The closed-loop adaptive diagnostics and therapeutic process begins when the onboard camera of the a-Heal wearable device captures an image of the wound and transmits it wirelessly to the a-Heal ML Physician. The ML Physician analyzes the image, generates a diagnosis of wound stage, and prescribes a treatment plan to accelerate wound healing. The wearable device receives the prescribed therapy wirelessly and implements it using bioelectronic actuators that deliver an electric field (EF) or a drug of choice (Fig. 1a). After the therapy takes effect for a specified duration, the wearable device captures a new wound image and restarts the diagnostic and therapeutic cycle (Fig. 1a). The wearable A-Heal includes a camera module, two printed circuit boards (PCBs) for camera illumination, onboard computing and wireless transmission, and a

transparent polydimethylsiloxane (PDMS) body that houses reservoirs for therapy storage and the bioelectronic actuators (Fig. 1b). A 3D-printed waterproof enclosure encases these components and integrates a USB-C port for connection to an external power supply (Fig. 1c). This enclosure attaches directly to a commercially available bandage, originally developed for Colostomy, ensuring a convenient and secure way to keep the device in place during treatment (Fig. 1c).

ML Physician
The goal of the ML Physician is to shift a wound from a slow or suboptimal healing trajectory to an accelerated path with the ultimate target of full closure (Fig. 2a). The ML physician achieves this shift with two main components: a Deep Mapper, a model used to find an optimal healing path with a Linear Quadratic Regulator (LQR), and a Deep Reinforcement Learning (DRL) controller (Fig. 2b)[19,20]. The Deep Mapper is comprised of an AutoEncoder (Fig. 2c) whose training is coupled with the learning of a linear model. That is, the weights on the encoder and decoder and the parameters of the linear model are optimized simultaneously. Let h be the encoder and h^{-1}, the decoder, then the linear dynamics $z_{k+1} = Az_k$, where $z_k = h(x_k)$, are achieved via minimizing the following loss:
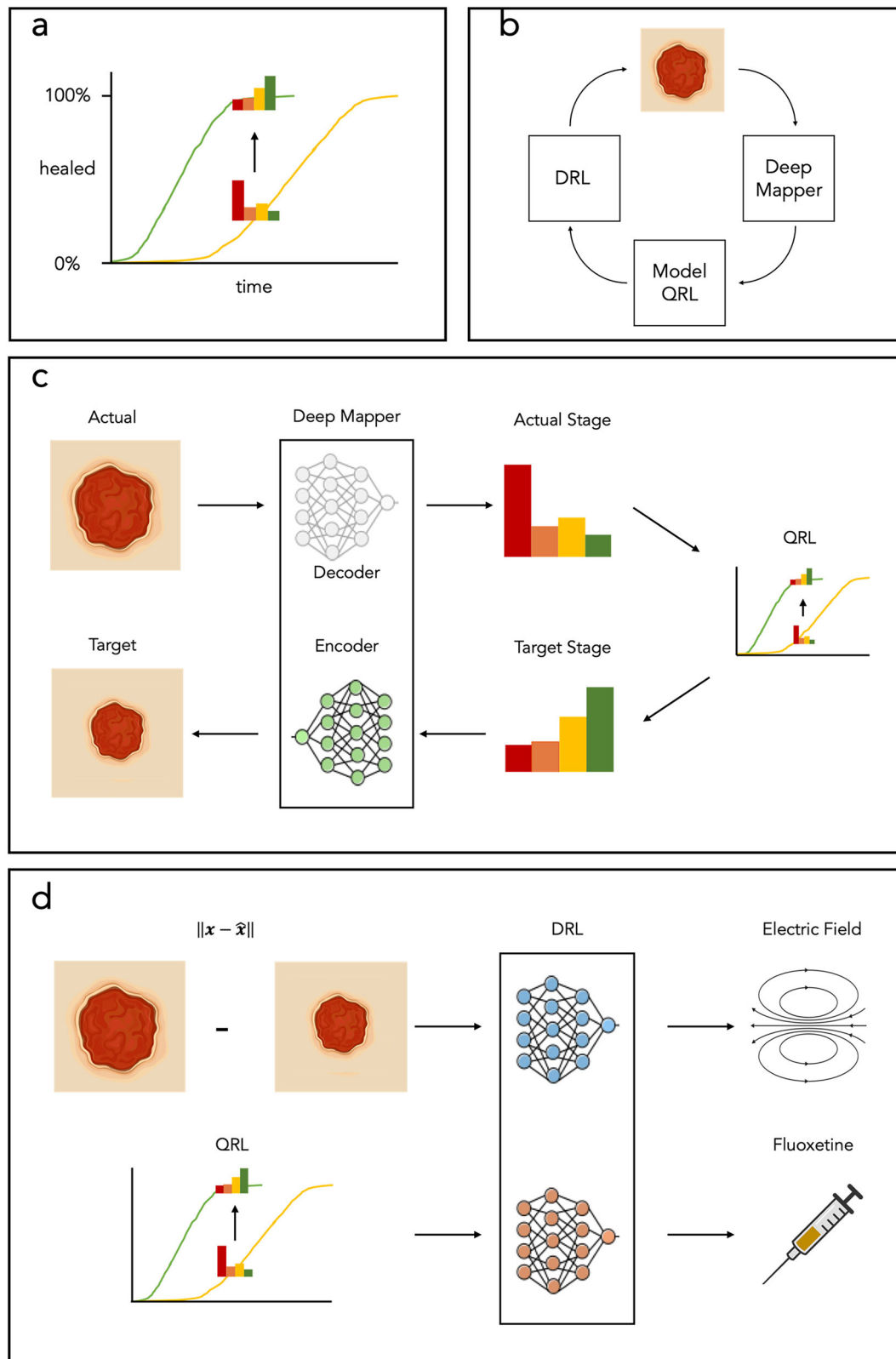
$$||h(x_{k+1}) - Ah(x_k)|| \qquad (1)$$

Fig. 2 | Schematic description of the ML Physician and its components. a Strategy for accelerating wound healing. **b** Control system components for wound healing acceleration Deep Mapper, Model with Quadratic Linear Regression (QRL), **c** functioning of deep mapper, **d** architecture for DRL to deliver optimal treatment.

Note that the encoder h maps the images to a four-state vector representing the wound state as probabilities across the four key healing stages: hemostasis, inflammation, proliferation, and maturation. The parameters in the matrix A represent the transition rates between these stages (e.g., hemostasis to inflammation, inflammation to proliferation, proliferation to maturation). The learned rates define the linear dynamic model[17], from which an optimal control law[21] are analytically derived using the LQR framework to minimize wound closure time. This control law takes
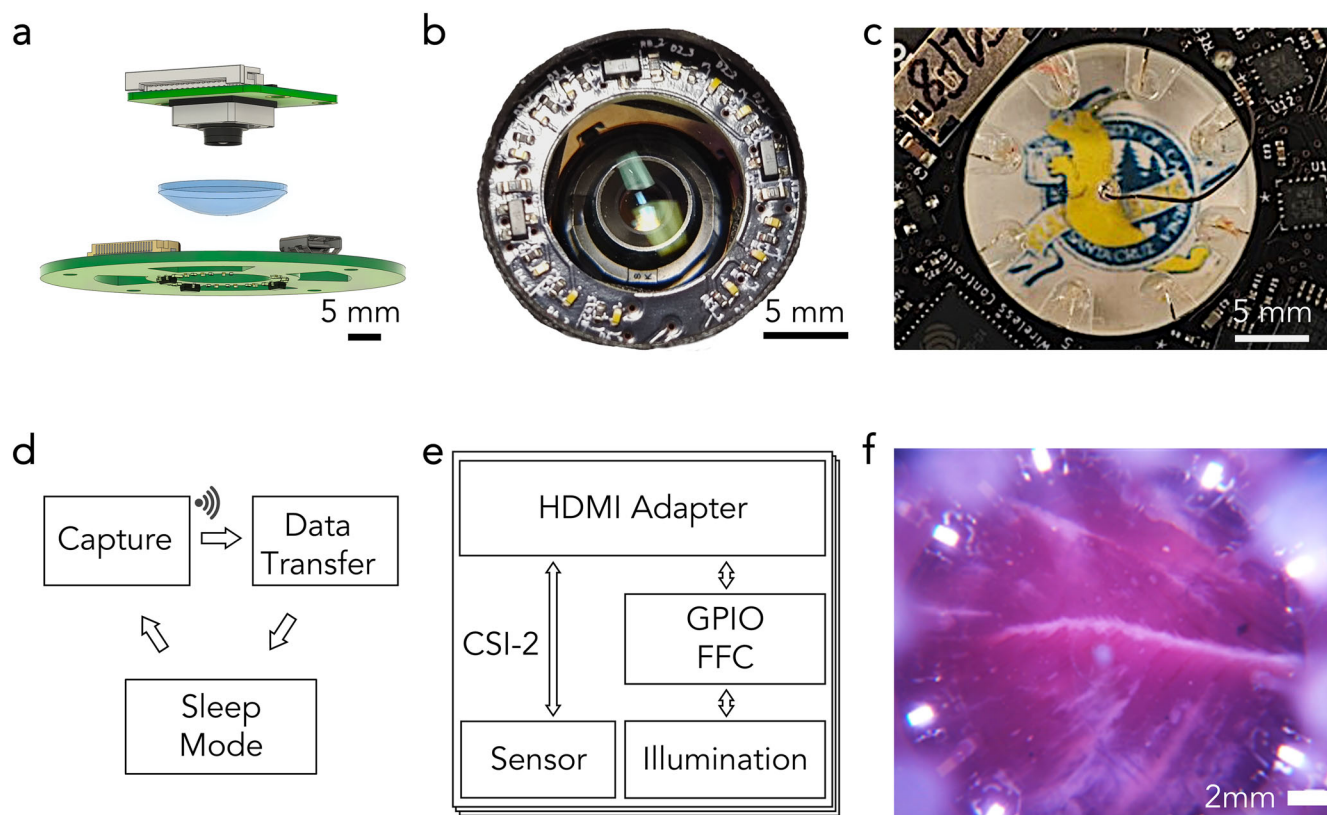
Fig. 3 | Overview of Imaging Subsystem and Key Components. a CAD of imaging components, **b** camera module with illumination board, **c** UCSC logo via PDMS optical path, **d** multi-day capture protocol, **e** controller communication via HDMI, CSI-2, GPIO, and I2C, **f** ex vivo porcine skin image from the device camera. optical path and the ion pump module device, and calibration target. **f** Sample wound image of an in vivo wound on a swine full thickness wound model.

the form $v_k = -Kz_k$. However, this LQR-derived optimal control is theoretical, representing adjustments to healing stages that minimize closure time but does not directly translate into actionable treatment parameters like EF strength and drug dosage. To address this limitation, we implement a leader-follower strategy[22], commonly used in robotic control[23], that combines the decoder with a DRL controller. The decoder generates a projected image of the wound, reflecting its predicted appearance if optimally treated according to the LQR model. This projected image acts as the "leader," representing the ideal healing outcome. The reward r of the DRL algorithm is the exponential of the negative Euclidean distance between the next wound image and the image generated by the linear state:

$$r(x_k, u_k) = \exp(-\eta||h^{-1}(z_{k+1}^*) - x_{k+1}||_2) \quad (2)$$

Here, $z_{k+1}^* = A^{nat}z_k - Kz_k$, is the four-state vector with values that should be achieved if the trajectory follows the optimal trajectory. The decoder maps the four-state vector to the image, which is compared to the actual image. This reward system updates the actor and critic parameters in the Actor-Critic (AC) Algorithm, which is used to select the treatment u_k in the next iteration based on the transition probability matrix $P(x_{k+1}|x_k, u_k)$, which represents the dynamics of the operating environment. In this experimental setup (Fig. 2d), two DRL controllers, referred to as "followers," are employed: one to determine the optimal fluoxetine (Flx) dosage and another to adjust the EF intensity. These controllers aim to minimize the discrepancy between the actual wound image (post-treatment with Flx or E_F) and the projected image, thereby ensuring that the healing process aligns closely with the optimized trajectory[17].

Camera module
Physicians rely on wound imaging for initial assessment as a critical tool for judging healing and guiding treatment decisions[24,25]. The A-Heal AI

Physician mimics the diagnostic approach used by physicians, enabling the creation of personalized treatment regimens[19,20]. To achieve this functionality, the a-Heal wearable device integrates an imaging module with a camera, a plano-convex lens, an illumination PCB, and a microcontroller (Fig. 3a and Supplementary Figs. 1 and 2). The illumination PCB, designed as a circular ring with 12 LED banks, surrounds the camera to ensure consistent lighting (Fig. 3b). The optical path from the wound to the camera passes through a transparent PDMS layer ($n = 1.4$), which incorporates the bioelectronic actuators and drug reservoirs[26]. A custom molding process ensures the PDMS achieves the optical clarity required for capturing high-quality wound images (Fig. 3c and Supplementary Figs. 3 and 4). The imaging module captures 11 images in a z-stack to optimize image quality by focusing on different planes and accommodating non-uniform biological surfaces. After capturing the images, the module transmits them wirelessly to a designated receiver and initiates a 2-h sleep mode before starting the next imaging cycle (Fig. 3d). The sleep mode is designed to minimize power usage and ensure that the batteries last at least 24 h, the typical wound monitoring cycle. The controller architecture integrates a microcontroller powered by a 5 V power bank, a CSI-2 multiplexer board, and shield boards. The microcontroller uses CSI-2 and GPIO/I2C interfaces to communicate with shield boards and links seamlessly with breakout boards, adapter boards, illumination PCBs, and imaging sensors through CSI-2 and HDMI connections (Fig. 3e). The module captures ex vivo images of swine skin and in vivo subcutaneous wound images (Fig. 3f). These images guide ML-based treatment algorithms and undergo post-processing to provide deeper insights into wound healing progression.

Bioelectronic therapy delivery
The second component of the a-Heal wearable—a set of bioelectronic actuators—enables on-demand therapy delivery and healing optimization (Fig. 4). This a-Heal wearable includes a ring-shaped PCB[27] and an
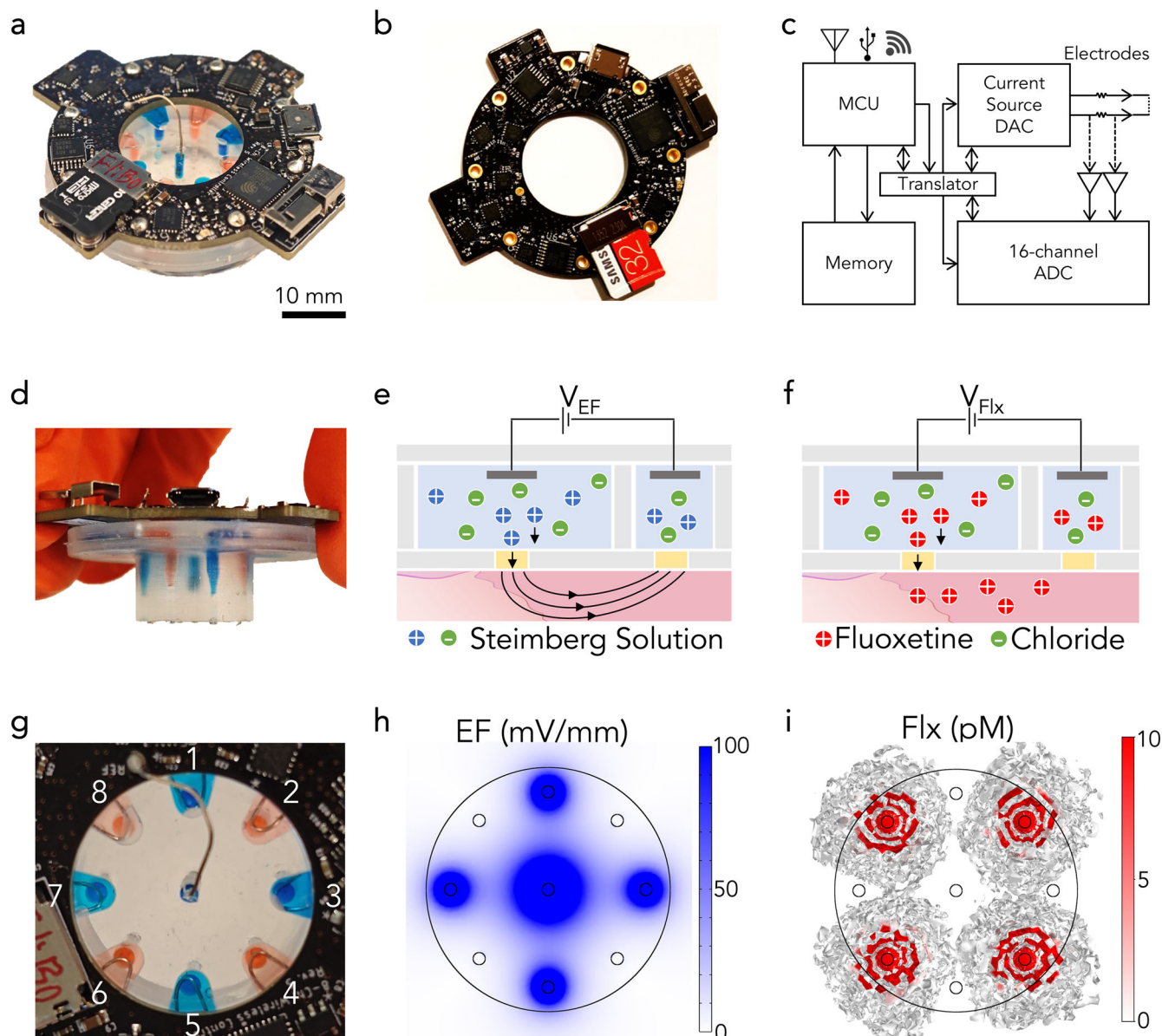
Fig. 4 | Setup of the bioelectronic actuator for electric field and iontophoretic drug delivery. a Actuator device photograph. **b** PCB with wireless potentiostat. **c** Microcontroller architecture, **d** Fluidic channel with dye solutions. **e** Fluoxetine delivery schematic. **f** Electric field delivery schematic. **g** Top view. **h** Fluoxetine dosage graph. **i** Electric field strength graph.

iontophoretic pump body with eight PDMS reservoirs (Fig. 4a)[28]. The PCB uses Wi-Fi to receive commands from the ML Physician and directs the microcontroller to initiate EF or FLX treatments (Fig. 4b). The microcontroller converts these commands into low-level signals, which the onboard potentiostat routes to specific iontophoretic pump channels by the analog-to-digital converters (ADCs) (V_{EF} for electric field, V_{Flx} for fluoxetine) (Fig. 4c).

The iontophoretic pump body contains four reservoirs for EF delivery (blue), four reservoirs for Flx (red) (Fig. 4d), and one reservoir in the center that hosts the counter/reference electrode[29]. Each reservoir contains Ag/AgCl electrodes and a capillary filled with an anionic polymer connects the reservoir to the wound bed(Supplementary Figs. 6 and 7)[30,31]. For EF delivery, the reservoirs contain sterile saline. For Flx delivery, the reservoirs contain a fluoxetine hydrochloride solution so that the Flx molecule has a net positive charge[32] (Supplementary Figs. 8 and 9)[33].

At V_{EF} = 4.7 V, the EF peaks at 400 mV/cm, as confirmed by COMSOL simulations (Fig. 4e and Supplementary Fig. 7) and from I_{EF} readings[31,34].

V_{FLX} drives fluoxetine from the reservoirs, across the capillaries, into the wound towards the wound center where the capillary with the counter/working electrode is located. The system measures I_{Flx} to estimate drug delivery, using HPLC to calibrate dose efficiency (Supplementary Figs. 8 and 9)[35]. Before each in vivo experiment, we conducted full in vitro and ex vivo validation (Supplementary Figs. 10–14). These current readings determine both the EF strength and the delivered fluoxetine dose[28,33,36].

Porcine wound healing

We deployed the a-Heal platform on a porcine excisional wound model in a preliminary evaluation of its effectiveness over a 22-day period[37]. The porcine excisional wound model is a well-established model with many similarities to human wounds. We evaluated a-Heal in combination with two pro-healing therapies with strong preclinical support: EF stimulation and Fluoxetine. EF is a well-established modality known to enhance wound healing by promoting directed cell migration, particularly of keratinocytes at the wound edge[30,31,38,39]. Application of EF at the wound margins—which is
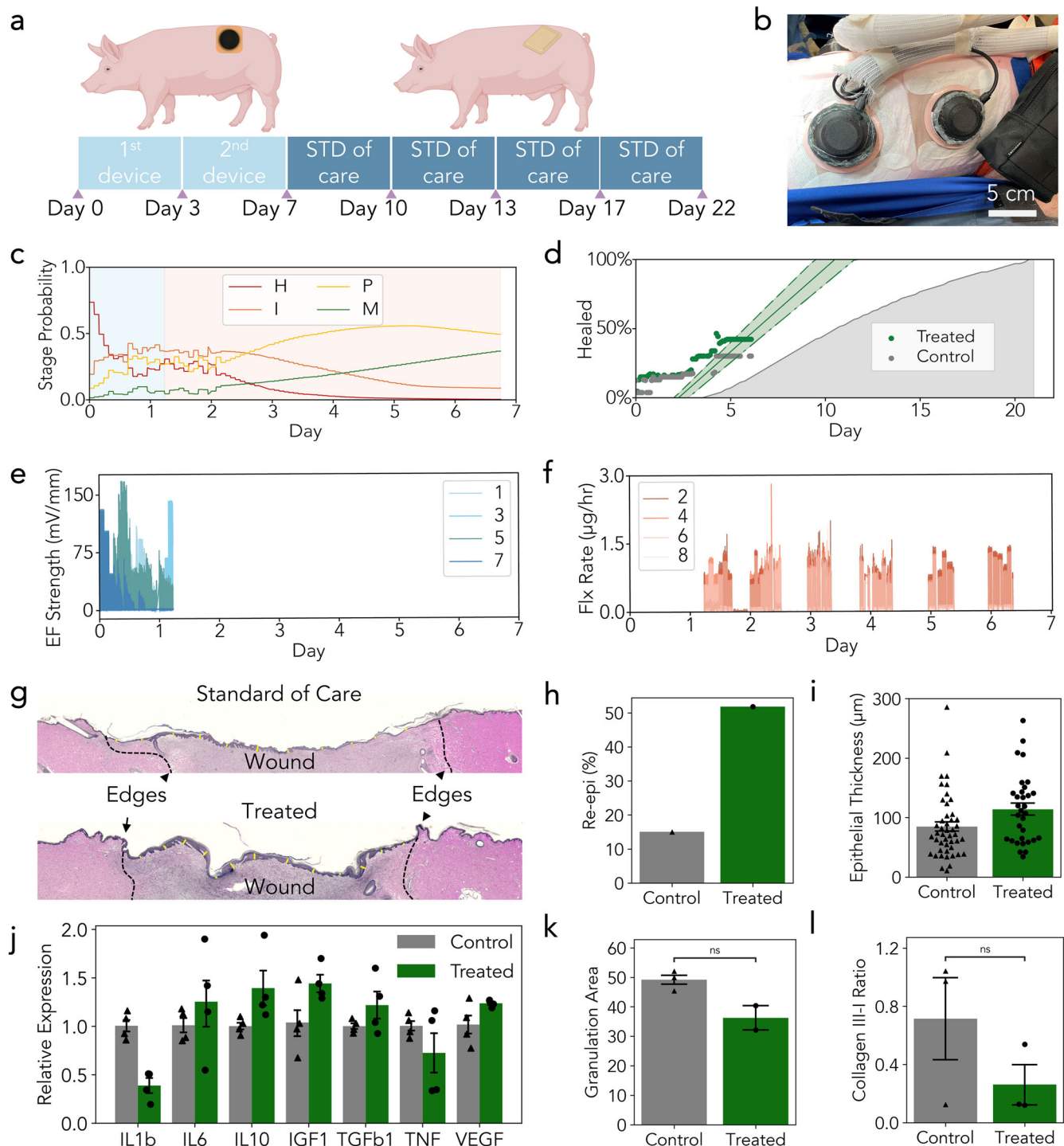
Fig. 5 | In Vivo study in porcine model for 22 days. a In vivo experiment schedule and setup. **b** photo showing the device was mounted on 20 mm wound of the porcine model. **c** wound stage probability of a treated wound, interpreted by Deep mapper. **d** Wound healing progress from control and treated wound, interpreted by Deep mapper. **e** Electric field strength from individual channels of a bioelectronic device. **f** Fluoxetine delivery rate from individual channels of a bioelectronic device. **g** Representative images from the day 22 wounds treated with standard of care (control) or the device. **h** re-epithelialization percentage of control vs treated wound at day 22, collected from Exp2, $n = 1$. **i** Epidermal thickness was measured on multiple sites across the neo-epithelium covering the three control wounds and two closed-loop treated wound ($n_{control} = 46$ technical replicates from 4 samples, $n_{treated} = 32$ technical replicates from 4 samples, $p = 0.026$). **j** RT- PCR analysis of gene expression from healed wound tissue collected on day 22. Expression of anti-inflammatory IL10 and pro-preparative TGFB1 have elevated in the device-treated wounds relative to the control standard of care ($n_{control} = 4$, $n_{treated} = 4$; IL10 increased by 39%, $p = 0.08$; IGF1 increased by 39%, $p = 0.08$; TGFb1 increase 22%, $p = 0.21$; VEGF increased 21%, $p = 0.10$). Genes associated with inflammation: IL1B, and TNFa are reduced (IL1b reduced by 61%, $p = 0.01$; TNF reduced 28%, $p = 0.27$; IL6 increased by 24%, $p = 0.44$) **k** Granulation tissue was identified by difference in histological staining and outlined and area measured. ($n_{control} = 3$, $n_{treated} = 2$, $p = 0.047$). **l** Ratio of collagen type III/I, derived from picrosirius red staining under polarized light from healed wounds at day 22. ($n = 3$, $p = 0.237$). Bar charts with error bars show the mean ± SD, with individual data points overlaid as dots, p values were calculated using a one-tailed Student's t-test.

largest at the onset of wounding and where the endogenous EF is strongest immediately post-injury—has been shown to accelerate re-epithelialization in a porcine wound model[40]. We have previously demonstrated that both topical[41] and bioelectronic delivery of Fluoxetine (Flx) significantly promote healing in a small animal model[33]. We chose to run the closed-loop therapy for the first 7 days, as earlier studies indicate that EF and Flx treatment from day 0 to day 7 promotes wound healing. After day 7, we removed the device and transitioned the wounds to standard[20,28] (Fig. 5a). We selected a 7-day treatment duration as a compromise between treatment efficacy, animal welfare, and the risk of device failure. Our previous studies[28,31,33] have shown that even brief treatment periods—as short as three days—can produce measurable improvements in wound healing[28,31,33]. In our current experiments, we observed a significant increase in device failure rates during longer protocols. This is largely due to porcine behavior, particularly in warmer months when animals roll in mud frequently to regulate body temperature. Such activity substantially raises the likelihood of device displacement or malfunction, thereby reducing the reliability and reproducibility of experimental data. For this proof-of-concept study, we therefore limited treatment to 7 days. Importantly, there are no inherent limitations preventing longer treatment durations in future studies, especially with a smaller and flexible device. The a-Heal wearable attached to a 20 mm wound on the porcine model supported the healing process (Fig. 5b and Supplementary Figs. S15–S17). Before operating the device on the porcine model, thorough biocompatibility tests confirmed its suitability (S10). We carried out two separate animal experiments (exp1 and 2); in each experiment, two wounds were treated with the a-Heal system, and four wounds served as control (Supplementary Fig. 18 and Table S3). The swine was able to freely move in its enclosure fitted with the devices and battery packs and underwent its normal routine (Supplementary Fig. 19). Throughout the closed-loop controlled treatment period (Day 0–7), the camera module captured high-resolution wound images every two hours (Supplementary Fig. 20), enabling the ML Physician to perform wound monitoring, diagnostics, and real-time decision-making for optimal therapy based on the wound's evolving condition. A laptop served as the server, granting access to a GUI through a web browser in clinical settings (Fig. 5c–f, Supplementary Figs. 21–24, and Table S3).

GUI displayed wound images (Supplementary Fig. 25), predicted wound stages, and healing rates compared to the control wound in the model, highlighting whether the wound progressed faster or slower (Fig. 5c, d). Drug delivery strategies were fully automated and also updated every 2 h. The algorithm chose a mostly steady rate of delivery, which has its advantages in the face of limited bioavailability. It also tracked device performance metrics, such as EF treatment data and drug dosage (Fig. 5e, f and Supplementary Figs. 21–26). In this care regimen, the A-Heal platform applied EF therapy until the treated wound's probability of inflammation increased to 40%, signaling progression toward the optimal healing trajectory. At this stage, A-Heal initiated Flx delivery, with the dosage determined by the AI Physician (Fig. 5c–f). EF stimulation effectively reduces the inflammatory phase[42], while FLX treatment promotes the proliferative phase[33,41]. To maximize the benefit of the two treatments, we initiate treatment with EF and transition to FLX when the ML algorithm detects that the wound is starting to transition from the inflammatory phase to the proliferative phase indicated when the probability of the inflammatory phase reaches its maximum point (derivative as a function of time is zero). The ML Physician is critical in this decision-making process, as wounds exit the inflammatory phase at different rates. Without ML guidance, premature FLX application may not reach the best healing effect. The ML Physician determines the treatment based on real-time wound healing data. This information directly informs the timing and dosage of EF and FLX treatments. In this homogeneous and controlled wound model, FLX dosing varied little across wounds. However, the onset of EF stimulation differed among the four wounds (Fig. 5c and SI, Supplementary Figs. 22–24), as each reached the inflammation threshold at a different time (26.0, 29.6, 45.8, 39.1 h, respectively)—consistent with expectations. In real-world scenarios, where wounds and patient responses are more heterogeneous, we anticipate that the ML Physician will recommend more personalized and variable treatment strategies. To further support this claim, additional in vivo studies will be necessary, including the same treatment regimen without ML physician input, as well as experiments using an infected wound model. Importantly, the ML Physician also imposes an upper limit on FLX dosing, as our data show that excessive FLX can impair, rather than promote, wound healing. In a clinical or remote care setting, the GUI allows physicians to intervene manually, fine-tuning treatments as needed (Supplementary Fig. 26). After the device removal on day 7, we continued to use a handhold optical camera to image the wound every 3 days to analyze the healing progress. The image shows that treated wounds show smaller wound areas during and at the end of the experiment (Figs. S27 and 28). Tissue analysis confirms that bioelectronic delivery of Flx is effective (Supplementary Fig. 29), and there is no systemic accumulation, reducing the chances of off-target effects (Supplementary Fig. 30). By day 22, during the late phase of wound healing, histomorphological analyses evaluated the regenerated tissue to determine wound resolution. Exp1 wounds achieved 100% re-epithelialization for all wounds, while exp2 reached 51.8% re-epithelialization on the treated wound and 15.0% for the control wound (Fig. 5h and Supplementary Fig. 31). The epidermal thickness on the treated wounds is 34.2% higher than the control, indicating further differentiation and maturation of the repaired tissue for treated wounds compared to the control (Fig. 5i and Supplementary Fig. 32). Additionally, the wound bed granulation tissue area decreased by 26.3% in device-treated wounds compared to those receiving standard care, indicating faster progression into the regeneration phase and improved resolution of granulation tissue (Figs. 5i and S31). Gene expression analysis using Qiagen RT2 qPCR Primers for pigs found that expression of anti-inflammatory IL10 and pro-preparative TGFB1 are elevated in the close-loop treated wounds relative to standard of care. Genes associated with inflammation: IL1B2, IL6, and TNFa are reduced in all healed wounds by day 22, indicating faster progress of healing with treatment (Fig. 5j and Table S3). Immunohistochemical (IHC) analysis of the numbers of nerve fibers in the epidermis of the imaged area captures enhanced innervation after combination treatment[43] and less angiogenesis (Supplementary Fig. 33), as well as a lower ratio of pro-inflammatory macrophages (M1) vs the pro-relatively macrophages (M2) (Supplementary Fig. 34). During normal wound healing, fibroblasts deposit type III collagen to the wound site first, and later the matrix is replaced by type I collagen[44]. Therefore, the ratio between the type III to type I collagen points to the progression of healing[45]. Here, we used Picrosirius Red staining under polarized light to quantify the two types of collagens (Fig. 5l and Supplementary Fig. 35). The decreased ratio in the device-treated wounds indicates a more mature collagen structure[45]. Treatment for two of the wounds was interrupted early due to device failure (Supplementary Figs. 23 and 24 and Table S3). This early interruption resulted in thinner epithelial thickness ($p = 0.023$), smaller granulation area and smaller collagen III/I ratio collectively confirming that a-Heal treatment driven by the ML physician indeed improves healing respect to manual healing (Fig. S36).

This study has several limitations. The in vivo sample size was modest, and the therapeutic agents, though effective in preclinical models, are not approved by the U.S. FDA for wound healing. Additionally, direct comparisons between ML-driven treatment, manual use of the device, and other clinically approved regimens beyond the standard of care are currently lacking. We focused exclusively on non-infected wounds, which do not capture the full complexity of clinical cases, and future studies in infected wounds will be necessary. Subsequent investigations will explore how the AI-guided closed-loop system performs in such wounds. The current device could be improved by miniaturizing the electronics, and a flexible platform could expand use to larger or irregular wounds[8,12,13]. Future work will refine the algorithm's decision-making, including automating the EF-to-FLX transition, which we manually set in this study. Although preliminary, this work demonstrates a functional framework that future studies must validate in larger, more diverse cohorts and clinically relevant conditions. A-Heal is an AI-powered adaptive wound healing platform that enables continuous monitoring, diagnostics, and personalized on-demand wound care. This

platform integrates ML image recognition to analyze simple images from an onboard camera, providing real-time wound diagnostics, with bioelectronic actuators that deliver personalized therapies, including EFs and drugs. a-Heal identifies wound stages and prescribes ad hoc therapies to guide each wound toward an optimal healing trajectory. A-Heal continuously reassesses the wound and dynamically adjusts the therapy to match the evolving healing process. Physicians can monitor progress remotely via a GUI, allowing for real-time assessment and intervention when needed. In a preliminary study with a clinically tractable large animal excisional wound model, A-Heal accelerated healing with a combined EF and fluoxetine therapy, showing improved epidermal thickness, reduced granulation tissue, improved collagen I/III ratios, and modulation of the inflammatory response. Notably, a-Heal driven by the ML physician, achieves higher and more consistent tissue concentrations of Flx in porcine excisional wounds compared to conventional topical bolus application, further supporting its integration into this therapeutic strategy[46]. The ML Physician uses a linear model trained to optimize transitions between wound healing phases and guide treatment. It improves healing outcomes over standard care, though it may not yet be fully optimized. In two cases where treatment was interrupted, wounds healed at rates slower than with continuous ML guidance, underscoring the importance of algorithm-driven treatment. Given the complexity of wound biology, random treatment combinations rarely accelerate healing. Data show that mistimed or misdosed FLX offers no benefit or worsens outcomes[46]. While the ML Physician may not always choose the optimal therapy and direct comparison with manual therapy is necessary, it continuously improves with each case, learning toward more effective strategies. Further in vivo optimization is impractical and potentially in silico studies may overcome this limitation. This wireless, portable system extends access to physician-guided therapy for patients in remote or underserved areas. Although tested in healthy animals, A-Heal shows potential to improve healing in chronic or diabetic wounds where natural repair is impaired.

Methods

A-Heal wearable camera module fabrication

The imaging subsystem consists of an Arducam camera module with UC-665 ribbon cable, a plano-convex lens, and a custom LED PCB ring, which are all housed within a 3D-printed enclosure. The enclosure components (bell top, lens holder, camera holder, LED PCB holder, and Bioelectronic Actuator holder) were fabricated using polylactic acid on a Prusa i3 3D printer. Each holder features alignment interfaces that enable stacking of components and their respective housings, as depicted in the CAD model of the wound healing device. Prior to assembly, the LED PCB ring is designed in KiCad and arrives fully assembled from Sierra Circuits. M2 metal threaded inserts are also heat-set into 3D-printed camera holder. The Arducam module is then secured to the camera holder using two 6 mm nylon M2 screws, and the UC-665 ribbon cable was inserted into the camera board.

Device assembly was performed under aseptic conditions in a Class II biosafety cabinet. All components underwent sterilization prior to assembly. Micro-HDMI cables were sterilized using a two-step protocol: thorough surface cleaning with 70% isopropyl alcohol (IPA) followed by UV irradiation for 15 min per side. Sterilized cables were stored in a stainless-steel container within the biosafety cabinet. Non-printed components were surface-sterilized with 70% IPA and UV-irradiated (15 min per side), while 3D-printed components were immersed in a 75:25 mixture of 99% IPA and deionized water prior to the UV exposure. The plano-convex lens was immersed in 70% IPA in a sterile polystyrene petri dish, with its curved surface oriented downward. Excess IPA was removed using non-woven wipes and silicon-tipped tweezers, followed by visual inspection to verify the absence of surface contamination.

Assembly proceeded sequentially under aseptic conditions. The LED PCB was positioned in its 3D-printed holder, with the micro-HDMI connector aligned with the access opening. The camera's ribbon cable was also connected to the LED PCB, followed by placement of the cleaned plano-

convex lens in its 3D-printed holder. The lens assembly, comprised of the lens and it's corresponding holder, was then stacked onto the LED PCB assembly. The camera assembly was mounted above the lens stack, and a sterile micro-HDMI cable was connected to the LED PCB port. The assembly was completed by positioning the bell-top enclosure and securing it to the LED PCB holder using thermoplastic adhesive applied to the holder's interfacing lip. The imaging subsystem is later combined with the bioelectronic actuator, its 3D-printed holder, and skin barrier to complete the integrated device.

A-Heal wearable PDMS body fabrication

The fabrication of the PDMS device involves molding three distinct components: the reservoir mold, the notch mold, and the channel piece. These molds are created using 3D printing and CNC milling techniques to achieve precision and consistency. Each of the molds is printed on a Formlabs 3B printer, using Model V3 resin with a layer thickness of 50 microns. To ensure optical clarity for the final device, a separate mold piece is fabricated from CNC-milled acrylic disks with a diameter of 19.5 mm. This step is critical for minimizing light scattering and optimizing the optical performance of the device.

The PDMS (Sylgard 184) mixture is prepared by combining the base and cross-linker in a 10:1 ratio. After thorough mixing, the mixture is degassed to remove trapped air, which helps prevent defects during molding. The prepared PDMS is then used to fill the reservoir and notch molds. The molds are carefully leveled and degassed again to ensure uniformity. Subsequently, they are cured at 60 °C for 48 h to ensure complete cross-linking and structural integrity. Once curing is complete, the PDMS components are extracted and undergo a cleaning process to remove any residual impurities. The components are sonicated in isopropanol (IPA), followed by thorough rinsing with water. Finally, the cleaned parts are oven-dried to prepare them for subsequent assembly.

Printed circuit board (PCB)

A customized PCB is designed and send to a vendor (PCB way) to manufacture. The PCB is ring-shaped, with an outer diameter of 43 mm and an inner diameter of 20 mm. The channels consist of eight plated through holes (PTHs), each 1.75 mm in diameter, arranged in a circular pattern at a radial distance of 19 mm from the center. These PTHs allow for mechanical and electrical integration with the PDMS ion pump piece beneath the PCB. The center reference channel is a 0.7 mm diameter PTH connected to the electrical ground of the PCB.

The actuator PCB is an 8-channel wireless device for electrical actuation and sensing, with an additional center channel serving as the electrical ground (reference). It uses a WiFi-capable, dual-core microcontroller unit (MCU), the ESP32-PICO-D4, to perform low-level processing and communication tasks between various onboard hardware components. A custom device firmware is loaded onto the flash memory of the MCU for this purpose. Each channel can provide an applied voltage of up to 3.3 V and an output current of up to 330 µA, depending on the load resistance at the channel. The applied voltage is controlled using an onboard 8-channel DAC53608 digital-to-analog converter (DAC). Voltages are measured by two onboard 8-channel ADS7828 ADCs. Op-amp voltage buffer amplifiers are used at the input of the ADCs to provide high input impedance for accurate current and voltage measurements. Current is determined by sensing the voltage across a high-precision (0.1%) 10 kΩ resistor in series with each channel. The onboard MCU uses the inter-integrated circuit (I²C) interface to send commands to the DAC and acquire data from the ADCs. Measured data is stored locally on a microSD card and wirelessly transmitted to a remote laptop via a 3D metal antenna. The MCU communicates with the microSD card using a serial peripheral interface and transmits data via WiFi using the TCP/IP protocol. Upon powering up, the PCB automatically connects to a local WiFi network set up with a commercial router. The remote laptop, also connected to the same network, sends high-level commands to the PCB for user-specified control, closed-loop operation, and real-time data acquisition. When the PCB receives a high-level command

from the laptop, the firmware breaks it down into a sequence of low-level tasks for the MCU to execute.

PCB integration and waterproof coating on actuators

Silver wires were inserted into each reservoir of the PDMS device to serve as working electrodes. These wires were then connected to the PCB. To ensure a proper seal, PDMS seals were applied at each insertion point and cured thoroughly. To assemble the device, custom-made aluminum clamps were used to hold the two parts of the device together during the plasma bonding process. The device parts were exposed to plasma for 10 s to activate the surfaces, after which the clamps were immediately bolted to secure the assembly. The entire device was subsequently heated at 60 °C for 30 min to facilitate bonding. The quality of the bonding was verified by injecting air into each reservoir and inspecting for any leaks. To protect the optical window of the device, adhesive tape was applied before the parylene coating process. The device was coated with a $2 \times g$ layer of parylene over a 3-h period, ensuring an even and durable protective layer. Once the PCB was attached, each wire was carefully soldered to the corresponding plate through holes on the board. A chlorinated silver wire was inserted into the central channel of the device to function as a counter electrode. Finally, a second layer of parylene coating was applied to provide additional protection and ensure the durability of the entire assembly.

Iontophoretic pump assembly

Capillaries (800 µm ID, CT95-03: TLC Spotting Capillary Tubes) were filled with NaOH for cleaning and subsequently conditioned using deionized water (MQ Water, 18.2 Ω), A174 silane coupling agent, and ethanol. This conditioning process was performed using a syringe pump to ensure consistent flow rates and thorough treatment of the inner surfaces. Following this, the capillaries were thoroughly dried to eliminate any residual solvents. The dried capillaries were then filled with the hydrogel precursor solution. Ultraviolet (UV) curing was applied to polymerize the hydrogel within the capillaries, using a UV intensity of 7 mW/cm² for an adequate curing time. The cured hydrogel-filled capillaries were cut into segments of 5 mm each. These segments were subsequently soaked in either Flx or Steinberg solution, depending on the intended application of each channel. For device preparation, reservoirs and channels were filled with the corresponding solution, Flx or Steinberg solution, based on whether the channel was designated for Flx or EF delivery. Capillary segments were inserted into each channel using a biopsy punch to create precise openings for integration. To ensure the structural integrity of the device, a biocompatible cap was 3D-printed and used to seal each channel effectively. This cap was specifically designed to prevent leakage and maintain a sterile environment.

Control software was loaded onto a custom PCB, allowing for accurate monitoring and regulation of the functions of the device. A thorough functionality test was performed to validate each aspect of the system, ensuring that it operated correctly before integration into the camera harness for experimental use.

The device and enclosure were then glued to a skin barrier (Hollister New Image™ Flat CeraPlus™ Skin Barrier—Tape,11204), which come with adhesive that can mount the device to the wound.

Deep learning models and algorithms in the ML Physician

The camera module captured wound images every 2 h throughout the experiment. DeepMapper was previously trained on mouse and porcine images that had high resolution and incorporated the whole wound. We fine-tuned DeepMapper to work with the device images after pre-processing of the images. Note that device images are substantially different than standard in vivo wound images, which have wound edge information and different color spectrum. To pre-process the images, we subtracted [108.16, 61.49, 55.44] from the pixel values of the RGB channels in the wound image to reduce redness, and we down-sample the image to shape (H: 128, W: 128, 3). The down-sampling method we are using is called Lanczos algorithm. Finally, we normalize pixel values to have zero mean and range from 0 to 1; The processed wound images were passed into the DeepMapper to predict

the wound's healing stage as well as the linear dynamics, based on which optimal reference signals were calculated. For the DRL application, only one DRL agent was active at a time. For example, when the DRL agent driving EF was active, all other channels associated with fluoxitine delivery were inactivated and vice versa. Initially, we used the agent controlling the EF; once the predicted healing probability reached approximately 40% and started to decrease, we switched to the DRL agent for fluoxetine delivery. Code is available on GitHub: DeepMapper: https://github.com/Fan-Lu/DeepMapper, for Deep Mapper; and https://github.com/Fan-Lu/RL4Wound for DRL.

Pig acclimation and wounding surgery

The Yorkshire-Landrace-Duroc cross breed pigs (30–55 Kg, young females) were ordered from the UCD Swine Research Center (Davis, CA). The procedure for swine care and the wounding surgery[37] were derived from the guidelines of the Association for Assessment and Accreditation of Laboratory Animal Care and the NIH Guide for the Care and Use of Laboratory Animals, reviewed, and approved by the UC Davis Campus Veterinary Services, and the UC Davis Institutional Animal Care and Use Committee. The animals were acclimated for 7–10 days, trained for saliva collection (saliva induced with fresh apple slices, and 0.5–1 mL collected with 4 large cotton swabs swiped across the mouth cavity in the morning before 12:30 p.m. for cortisol measurement by HPLC), harness use (Kruz Original Heavy-Duty No Pull Dog Harness, medium to extra-large sizes), and human contact with positive reinforcement (food treats), and fasted for 15 h the night before the surgery. Anesthesia induction was with Telazol (5.5 mg/kg, intramuscular injection), followed by masked inhalation of Isoflurane (1–5% to effect). Then the pig was intubated, and body temperature, heart rate, and respiratory rate were monitored every 15 min. The pig blood samples were collected from the ear vein (up to 10 mL per collection) for plasma and serum isolation. The dorsal skin was shaved, hair-removed with depilation cream, and prepared with 2% chlorhexidine scrubs and IPA rinses. Prophylactic antibiotic (Cefazolin, 30–35 mg/Kg via IV) was injected during the wounding surgery.

Six circular wounds (20 mm in diameter, at least 50 mm apart to fit the device and skin barrier) were created with a scalpel blade and scissors down to the desired depth (partial thickness wounds, 6 mm deep) on the paravertebral area of a pig. After compression hemostasis, wound images were captured with a cell phone camera (iPhone 7, Apple) held at a constant distance of 10 cm above the wound, with a wound scale (Medline NE1 Wound Assessment Tool). The wounds were rinsed with a 0.001% cefazolin and then received standard care or the sterile devices (device-treated). The standard care wounds were covered with Conformant 2 Wound Veil (Smith & Nephew, Watford, England, UK), a hydrophilic polyurethane foam dressing, Optifoam (Medline, Illinois, USA), and a transparent dressing, Tegaderm (3 M, Minnesota, USA). The devices were pre-tested for Wi-Fi connection and applied to the wounds. The skin barrier adhesive dressing on the devices was further secured with MedFix Dressing Retention Tape (Medline). The entire dorsum of the animal with the wounded area was protected with foam sheets (3 M, Reston self-adhering foam pad) in a spandex tube (Showpro Lamb tube) with Velcro openings on the back to access the wounds. The devices were connected to the power bank (Voltaic Systems V75) and the Raspberry Pi (model 4B) controller, carried in 2 pouches (Tacticool Molle) attached to the shoulder harness on the pig. The exposed wires between the devices and the pouches were covered with cord protector tubing to prevent chewing by the animal. Post-operative analgesic (buprenorphine, 0.005–0.1 mg/kg intramuscular injection before extubation; fentanyl patch, 1–5 µg/kg/h for 72 h) was given at the end of the surgery, and the pig was monitored for signs of hyperthermia after recovery.

a-Heal wearable actuation

The a-Heal wearable were connected to a designated wifi network (Supplementary Figs. 15 and 16), set up in the vivarium. The researchers operate the device through wireless command from the laptop computer.

Camera control and image acquisition were implemented using libcamera on Linux, which enables command-line configuration of the Arducam module. The imaging protocol consists of three scripts: a preview script using continuous image capture for real-time monitoring, an acquisition script with various parameters for use during experiments, and a validation script that performs automated capture of six sequential images in a 24-h stress test cycle. The image acquisition parameters include a 70 s initialization delay to ensure system stability and network connection, followed by 3 s programmed delay between image captures. The focal parameter is varied from representative values 0 to 5 to capture z-stack images, with a value of 3 corresponding to the theoretical focal plane. Each Raspberry Pi unit is configured with a unique camera identifier corresponding to its designated wound site, and automated image transfer to remote storage is implemented using an IP address. The system includes an automated shutdown protocol for reduced power consumption post-acquisition during in vivo experiments.

The actuator automatically connects to Wi-Fi and enters standby mode. A software module, incorporating the Deepmapper and DRL algorithm, runs on a laptop, sending commands to the actuator. The module includes a user-friendly GUI that allows researchers to monitor and interact with the system. The software automatically stops the actuator when the target treatment is achieved, or the set duration expires.

To maintain consistency across experiments, the device and software operate for 22 h daily, with a 2-h window allocated for data transfer, battery replacement, and routine checks. The battery (Voltaic Systems V75), which can support 36 h of operation, is typically replaced daily to ensure uninterrupted power. After each battery change, the software module is manually reset, and data are copied to the laptop's hard drive. This process is repeated daily throughout the experiment.

Post-operative care
The wounds and the devices were examined daily. The wound device and dressings were replaced every 3–4 days over the course of the experiments. At the end of observation on postoperative day 22, a blood sample was again collected, and the animal was euthanized. Wound tissue was excised with a 10 mm margin of surrounding intact skin, bisected along the axis of the device actuation and the channels reaching the targeted treatment concentration, formalin-fixed, paraffin-embedded (FFPE), and sectioned to 5 μm for H&E staining and immuno-histochemistry (IHC).

Wound epithelialization
Wound tissues were fixed in 4% paraformaldehyde for one week, embedded in paraffin blocks (Tissue Tek processing and embedding stations, Sakura Finetek, Torrance, California) and 5 μm-thick sections were affixed to glass slides. After drying, the sections were stained to visualize neo-epithelium, collagen deposition, neurons, or macrophages. Tissue sections were stained using a standard H&E protocol to assess re-epithelialization as previously described[37]. Stained sections were imaged using a BZ-9000 inverted microscope, and the images were scored in the BZ-II Analyzer software (Keyence, Osaka, Japan). The wound edge was identified by the absence of subcutaneous fat and muscle and by the visible demarcation between the granulation tissue and mature dermal collagen. Re-epithelialization was measured along the basal keratinocytes, and the percentage was calculated by the length of the neo-epithelium from both edges and the total length of the wound.

Picrosirius red staining and collagen ratio
Five-micron wound sections were stained with Picrosirius Red solution (American MasterTech/StatLab, McKinney, TX) for 1 h, destained with acidic alcohol according to the manufacturer's instruction, and imaged under polarized light[47] on a BioRevo BZ-9000 inverted microscope (Keyence, Japan) with the BZ-Viewer and BZ-Analyzer software (Keyence, Japan). Color extraction of type I collagen (red to orange color) and type III collagen (green to yellow color) was performed with the "hybrid cell-count" function in the BZ-Analyzer. The area of the two types of collagen in the wound bed (identified by H&E staining in a sequential section) was quantified in each section for the collagen III to I ratios. High ratio of collagen III indicates newly regenerated granulation tissue, whereas high ratio of collagen I suggests well re-organized, mature dermal tissue.

Cortisol extraction from saliva and chromatographic analysis
Pig saliva was expressed from the cotton swabs and centrifuged to remove particulate matter. The clarified saliva was divided into aliquots and stored at −80 °C until analysis. Samples were extracted according to a method described by Hofreiter et al. (PMID: 7147286), modified for measurement of cortisol in saliva. Briefly, 0.300 mL saliva was shaken for 3 min with 1.000 mL dichloromethane. The aqueous phase was removed, and the dichloromethane layer was washed by shaking for 1 min with 0.100 mL 0.1 N NaOH followed by 0.100 mL water. After each step, the samples were centrifuged to induce phase separation, and the aqueous phase was removed by aspiration. The dichloromethane layer was transferred to a clean tube and evaporated at 40 °C under a gentle stream of nitrogen. The residue was reconstituted in 100 μL of 50:50 methanol: water, and 10 μL was injected for analysis.

Measurements were performed using reverse-phase HPLC with UV absorbance detection. The system was an Antec Neurotransmitters Analyzer coupled to a Knauer BlueShadow 40D detector. Separation was performed on a Waters Acquity UPLC BEH C18 column (3.0×100 mm, 1.7 μm) at a flow rate of 0.450 mL per minute and a temperature of 35 °C. The mobile phase consisted of 28:72 acetonitrile: water, and column effluent was monitored at 242 nm.

Extraction of fluoxetine and norfluoxetine from pig plasma
Pig plasma samples were purified prior to analysis using C18 cartridge solid-phase extraction (SPE). 100 mg C18 cartridges were packed into glass SPE tubes with glass fiber frits (Macherey-Nagel, Duren, Germany). The sorbent was taken from Sep-Pak Plus 360 mg C18 cartridges (Waters, Ireland), which were broken open. Plasma extraction was carried out as follows: cartridges were placed onto a vacuum manifold and conditioned with two tube volumes of methanol and one tube volume of water. Pig plasma (0.500 mL) was spiked with 50.0 μL internal standard solution (40.0 μg/mL fluvoxamine in methanol), diluted with 0.500 mL H_2O, and this was passed through the conditioned SPE cartridges. Next, cartridges were rinsed with one tube volume H_2O followed by one tube volume 50:50 methanol: H_2O. Fluoxetine and norfluoxetine were eluted from the cartridges in 0.500 mL methanol containing 0.5% (v/v) formic acid, the eluate was made up to 1.000 mL by addition of 0.500 mL H_2O, and 10 μL of this was injected for analysis.

Immunohistochemistry staining of pig skin
FFPE skin sections from day 23 were used for immunohistochemistry (IHC) staining to visualize macrophages, neurons, and angiogenesis. Macrophages were labeled with antibodies against iNOS (M1; ThermoFisher, Catalog # PA1-036), arginase 1 (M2; ThermoFisher, Catalog # PA5-18392), and a pan-macrophage marker (BA4D5; Bio-Rad, Catalog # MCA2317GA). Multicolor labeling was achieved using donkey anti-goat Alexa Fluor 568 (Invitrogen, Catalog # A-11057), donkey anti-rabbit Alexa Fluor 647 (Invitrogen, Catalog # A-31573), and donkey anti-mouse Alexa Fluor 488 (Invitrogen, Catalog # R-37114). Neurons were identified in consecutive skin sections of 30 μm thickness using the PGP9.5 antibody (ThermoFisher, Catalog # 480012) and donkey anti-mouse Alexa Fluor™ 488 (Invitrogen, Catalog # R37114) as the secondary antibody. Angiogenesis was assessed with the CD31 (PECAM-1) antibody (Cell Signaling, Catalog # 77699S), followed by donkey anti-rabbit Alexa Fluor 647 (Invitrogen, Catalog # A-31573). All slides were mounted with VECTASHIELD® Antifade Mounting Media with DAPI (Vector Laboratories, Catalog # H-1200-10) for nuclei visualization. Imaging was performed with a Zeiss LSM900 Confocal Laser Scanning Microscope at a resolution of 3 pixels per μm. For each wound sample, three stitched images of the wounded region near the healed epidermis were collected using a 40× oil immersion lens to minimize tissue

variation. Quantification of macrophages, neurons, and blood vessels was performed by visualizing the staining in the confocal images, and analysis was carried out accordingly.

Extraction of serotonin from pig plasma

Prior to analysis, pig plasma samples were depleted of protein as follows: pig plasma (0.100 mL) was spiked with 5.00 μL antioxidant solution (1.3% (m/v) ascorbic acid and 2 mM EDTA in H_2O) and 20.00 μL internal standard solution (300.0 μM N-methylserotonin in H_2O). Next, 5.64 μL of 70% perchloric acid solution (Thermo Scientific, Waltham, Massachusetts) was added and the samples were vortexed for 30 s. The samples were centrifuged, and 10 μL of the supernatant was injected for analysis.

Fluoxetine concentration measurement from wound tissue

Pig wound tissues (20.0 to 30.0 mg) were cryo-pulverized over liquid nitrogen, resuspended in 0.250 mL methanol containing 0.5% (v/v) formic acid, and sonicated for 15 min in a sonicating bath. The tissue homogenates were centrifuged, the supernatants were made up to 0.500 mL by addition of 0.250 mL water, and 10 μL of the finished extract was injected for analysis.

Measurements were performed using reverse-phase HPLC with UV absorbance detection. Separation was performed on an Acquity UPLC BEH C18 column (3.0 mm ID × 100 mm L, 1.7 μm particles) at a flow rate of 0.450 mL per minute and a column temperature of 35 °C. The mobile phase consisted of 35:65 acetonitrile: 45 mM phosphate buffer pH = 6.0, and column effluent was monitored at 230 nm.

Chromatographic analysis of fluoxetine, norfluoxetine, and serotonin

Measurements were performed using reverse-phase HPLC with UV absorbance detection. The system was an Antec Neurotransmitters Analyzer coupled to a Knauer BlueShadow 40D detector. Separation was performed on a Waters Acquity UPLC BEH C18 column (3.0 × 100 mm, 1.7 μm) at a flow rate of 0.450 mL per minute. For fluoxetine and norfluoxetine analysis, the mobile phase consisted of 35:65 acetonitrile: 45 mM phosphate buffer pH = 6.0, separation was performed at 35 °C, and the column effluent was monitored at 230 nm. For serotonin analysis the mobile phase consisted of 4:96 acetonitrile: 50 mM citrate buffer pH = 4.3, separation was carried out at 37 °C, and the column effluent was monitored at 275 nm.

Gene expression and qPCR

Wound tissue was preserved in Invitrogen RNALater Stabilization Solution (Fisher Scientific) at 4° for 4 days and frozen at −80° according to the manufacturer's instructions. The frozen tissue was trimmed with a 5 mm biopsy punch from the wound edge (50 mg tissue), minced to 1 mm pieces, and homogenized with Tissue Tearor (BioSpec cat# 98537004) in 300 μl Buffer RLT containing β-mercaptoethanol (Qiagen RNeasy Fibrous Tissue Mini Kit) on ice for 2 min. The mRNA was extracted with Qiagen RNeasy Fibrous Tissue Mini Kit, and cleaned with DNase I according to the manufacturer's instructions. One μg of RNA was reverse transcribed to cDNA using the Quantitect Reverse Transcription Kit (Qiagen). The following Qiagen RT2 qPCR Primer for pigs were used: IL1B2 (PPS00015A-200), IL6 (PPS00991A-200), IL10 (PPS00445B-200), IGF1 (PPS00801A-200), TGFB1 (PPS00418A-200), TNF (PPS00426A-200), VEGFA (PPS00495A-200), NOS2 (PPS00221A-200), ARG1 (PPS00454A-200), DCX (PPS14382A-200), MAP2 (PPS02696A-200), COL1A1 (PPS72004A-200), COL3A1 (PPS02256A-200), RPL19 (PPS00333A-200), and GAPDH (PPS00192A-200). For qPCR analysis, the Quantitect Sybr Green master mix was used (Qiagen) on a 384-well platform (Bio-Rad CFX384 Real-Time System, C1000 Touch Thermal Cycler). Each sample was run in duplicate and mRNA levels of target genes were normalized to the average levels of housekeeping genes GAPDH and RPL19. Relative expression of the target gene was calculated via ΔΔCt against the average Ct of the housekeeping genes and the average Ct of day 0 skin from each animal.

Statistic analysis

Statistical analysis was performed using multiple software packages, including Microsoft Excel, the Scipy.stats library written in Python. P values were calculated using a one-tailed Student's t-test. The fold change dataset was analyzed by the Grubbs Test to remove outliers and by the t-test to determine statistical significance.

Data availability

No datasets were generated or analysed during the current study.

Code availability

Codes were shared open source on GitHub with the following link: Deep mapper for wound stage analysis (https://github.com/Fan-Lu/DeepMapper); Deep reinforced learning decision maker (https://github.com/Fan-Lu/RL4Wound).

References

1. Research, G. V. *Wound Care Market Size & Share | Industry Report, 2025-2030*. (Grand View Research, 2024).
2. Sen, C. K. Human wound and its burden: updated 2022 compendium of estimates. *Adv. Wound Care* **12**, 657–670 (2023).
3. Mirhaj, M., Labbaf, S., Tavakoli, M. & Seifalian, A. M. Emerging treatment strategies in wound care. *Int. Wound J.* **19**, 1934–1954 (2022).
4. Beyene, R. T., Derryberry, S. L. & Barbul, A. The effect of comorbidities on wound healing. *Surg. Clin.* **100**, 695–705 (2020).
5. Petzschner, F. H. Practical challenges for precision medicine. *Science* **383**, 149–150 (2024).
6. Freedman, B. R. et al. Breakthrough treatments for accelerated wound healing. *Sci. Adv.* **9**, eade7007 (2023).
7. desJardins-Park, H. E., Gurtner, G. C., Wan, D. C. & Longaker, M. T. From chronic wounds to scarring: the growing health care burden of under- and over-healing wounds. *Adv. Wound Care* **11**, 496–510 (2022).
8. Wang, C., Shirzaei Sani, E. & Gao, W. Wearable bioelectronics for chronic wound management. *Adv. Funct. Mater.* **32**, 2111022 (2022).
9. Razzaghi, M. et al. Remote-controlled sensing and drug delivery via 3D-printed hollow microneedles. *Adv. Healthc. Mater.* **13**, 2400881 (2024).
10. Saghazadeh, S. et al. Drug delivery systems and materials for wound healing applications. *Adv. Drug Deliv. Rev.* **127**, 138–166 (2018).
11. Lee, S. Y. et al. Combinatorial wound healing therapy using adhesive nanofibrous membrane equipped with wearable LED patches for photobiomodulation. *Sci. Adv.* **8**, eabn1646 (2022).
12. Jiang, Y. et al. Wireless, closed-loop, smart bandage with integrated sensors and stimulators for advanced wound care and accelerated healing. *Nat. Biotechnol.* **41**, 652–662 (2023).
13. Shirzaei Sani, E. et al. A stretchable wireless wearable bioelectronic system for multiplexed monitoring and combination treatment of infected chronic wounds. *Sci. Adv.* **9**, eadf7388 (2023).
14. Dargaville, T. R. et al. Sensors and imaging for wound healing: a review. *Biosens. Bioelectron.* **41**, 30–42 (2013).
15. Douville, C. et al. Machine learning to detect the SINEs of cancer. *Sci. Transl. Med.* **16**, eadi3883 (2024).
16. Swanson, K., Wu, E., Zhang, A., Alizadeh, A. A. & Zou, J. From patterns to patients: advances in clinical machine learning for cancer diagnosis, prognosis, and treatment. *Cell* **186**, 1772–1791 (2023).
17. Lu, F., Zlobina, K., Rondoni, N. A., Teymoori, S. & Gomez, M. Enhancing wound healing through deep reinforcement learning for optimal therapeutics. *R. Soc. Open Sci.* **11**, 240228 (2024).
18. Dallmann, A. C., Sheridan, M., Mattke, S. & Ennis, W. Prediction of healing trajectory of chronic wounds using a machine learning approach. *Adv. Wound Care* https://doi.org/10.1089/wound.2024.0095 (2024).

19. Lu, F. et al. DeepMapper: attention-based autoencoder for system identification in wound healing and stage prediction. Preprint at *bioRxiv* https://doi.org/10.1101/2024.12.17.628977 (2024).

20. Lu, F. et al. Accelerating wound healing through deep reinforcement learning: a data-driven approach to optimal treatment. *Bioengineering* **12**, 756 (2025).

21. Bertsekas, D. *Dynamic Programming and Optimal Control: Volume I* (Athena Scientific, 2012).

22. Mutz, F. et al. Following the leader using a tracking system based on pre-trained deep neural networks. In IEEE *2017 International Joint Conference on Neural Networks (IJCNN)* https://doi.org/10.1109/IJCNN.2017.7966404 (2017).

23. Saridis, G. Intelligent robotic control. *IEEE Trans. Autom. Control* **28**, 547–557 (1983).

24. Carrión, H. et al. HealNet - Self-supervised Acute Wound Heal-Stage Classification. In: Lian, C., et al. (eds) *Machine Learning in Medical Imaging. MLMI 2022. Lecture Notes in Computer Science,* vol 13583 https://doi.org/10.1007/978-3-031-21014-3_46 (Springer, Cham, 2022).

25. Wu, Y., Wu, L. & Yu, M. The clinical value of intelligent wound measurement devices in patients with chronic wounds: a scoping review. *Int. Wound J.* **21**, e14843 (2024).

26. Hee, W. S. et al. Design and validation of a wearable imaging system for automated wound monitoring in porcine model. Preprint at *bioRxiv* https://doi.org/10.1101/2024.12.18.629174 (2024).

27. Baniya, P. et al. Wireless bioelectronic device for wound healing. Preprint at *bioRxiv* https://doi.org/10.1101/2024.12.18.629068 (2024).

28. Li, H. et al. Remote-controlled wireless bioelectronics for fluoxetine therapy to promote wound healing in a porcine model. *Adv. Mater. Technol.* https://doi.org/10.1002/admt.202500040 (2025).

29. Jia, M., Luo, L. & Rolandi, M. Correlating ionic conductivity and microstructure in polyelectrolyte hydrogels for bioelectronic devices. *Macromol. Rapid Commun.* **43**, 2100687 (2022).

30. Zhao, M. Electrical fields in wound healing—An overriding signal that directs cell migration. *Semin. Cell Dev. Biol.* **20**, 674–682 (2009).

31. Hernandez, C. O. et al. A bioelectronic device for electric field treatment of wounds reduces inflammation in an in vivo mouse model. *PLoS ONE* **19**, e0303692 (2024).

32. Garrido, E. M., Garrido, J., Calheiros, R., Marques, M. P. M. & Borges, F. Fluoxetine and norfluoxetine revisited: new insights into the electrochemical and spectroscopic properties. *J. Phys. Chem. A* **113**, 9934–9944 (2009).

33. Li, H. et al. Programmable delivery of fluoxetine via wearable bioelectronics for wound healing in vivo. *Adv. Mater. Technol.* **9**, 2301115 (2024).

34. Reid, B., Song, B., McCaig, C. D. & Zhao, M. Wound healing in rat cornea: the role of electric currents. *FASEB J.* **19**, 379–386 (2005).

35. Juan, H., Zhiling, Z. & Huande, L. Simultaneous determination of fluoxetine, citalopram, paroxetine, venlafaxine in plasma by high performance liquid chromatography–electrospray ionization mass spectrometry (HPLC–MS/ESI). *J. Chromatogr. B* **820**, 33–39 (2005).

36. Marquez, G. et al. Delivering biochemicals with precision using bioelectronic devices enhanced with feedback control. *PLoS ONE* **19**, e0298286 (2024).

37. Yang, H. Y. et al. Combination product of dermal matrix, preconditioned human mesenchymal stem cells and timolol promotes wound healing in the porcine wound model. *J. Biomed. Mater. Res. B Appl. Biomater.* **110**, 1615–1623 (2022).

38. Song, B. et al. Application of direct current electric fields to cells and tissues in vitro and modulation of wound electric field in vivo. *Nat. Protoc.* **2**, 1479–1489 (2007).

39. Zhao, M., Rolandi, M. & Isseroff, R. R. Bioelectric signaling: role of bioelectricity in directional cell migration in wound healing. *Cold Spring Harb. Perspect. Biol.* **14**, a041236 (2022).

40. Liang, Y. et al. Application of stable continuous external electric field promotes wound healing in pig wound model. *Bioelectrochemistry* **135**, 107578 (2020).

41. Nguyen, C. M. et al. Topical fluoxetine as a novel therapeutic that improves wound healing in diabetic mice. *Diabetes* **68**, 1499–1507 (2019).

42. Gürgen, S. G., Sayın, O., Çetin, F. & Tuç Yücel, A. Transcutaneous electrical nerve stimulation (TENS) accelerates cutaneous wound healing and inhibits pro-inflammatory cytokines. *Inflammation* **37**, 775–784 (2014).

43. Brown, M. A., Troyer, J. L., Pecon-Slattery, J., Roelke, M. E. & O'Brien, S. J. Genetics and pathogenesis of feline infectious peritonitis virus. *Emerg. Infect. Dis.* **15**, 1445–1452 (2009).

44. Mathew-Steiner, S. S., Roy, S. & Sen, C. K. Collagen in wound healing. *Bioengineering* **8**, 63 (2021).

45. Gardeazabal, L. & Izeta, A. Elastin and collagen fibres in cutaneous wound healing. *Exp. Dermatol.* **33**, e15052 (2024).

46. Gallegos, A. et al. Fluoxetine delivery for wound treatment through an integrated bioelectronic device – pharmacokinetic parameters and safety profile in swine. Preprint at *bioRxiv* https://doi.org/10.1101/2025.03.11.642735 (2025).

47. Coelho, P. G. B., Souza, M. V., Conceição, L. G., Viloria, M. I. V. & Bedoya, S. A. O. Evaluation of dermal collagen stained with picrosirius red and examined under polarized light microscopy. *An. Bras. Dermatol.* **93**, 415–418 (2018).

Acknowledgements

Author contributions

Conceptualization: M.R., R.I., M.G., M.T., M.Z. Methodology: M.R., R.I., M.G., M.T., H.Y., A.S., M.Z., H.L., F.L., W.H., N.A. Investigation: H.L., H.S., F.L., W.H., N.A., P.B., A.G., K.S., K.Z., C.R., M.T., M.K., G.K., T.N., S.F., C.F., K.D., A.B., S.C., A.E., K.L. Visualization: H.L., G.L., S.K. Funding acquisition: M.R., R.I., M.G., M.T., M.Z. Project administration: M.R., E.A. Supervision: M.R., R.I., M.G., M.T., M.Z., A.S. Writing–original draft: H.L., G.L., S.K., H.S., M.R., M.T., M.T., M.G., F.L., R.I. Writing–review & editing: M.R., R.I., M.G., M.T., M.Z., A.S.

Competing interests

The authors declare no competing interests.

Additional information